# Anti-resonance features of destructive quantum interference in single-molecule thiophene junctions achieved by electrochemical gating

Jie Bai[1,5], Abdalghani Daaoub[2,5], Sara Sangtarash[2,5], Xiaohui Li[1,5], Yongxiang Tang[1], Qi Zou[3], Hatef Sadeghi[2], Shuai Liu[1], Xiaojuan Huang[1], Zhibing Tan[1], Junyang Liu[1], Yang Yang[1], Jia Shi[1], Gábor Mészáros[4], Wenbo Chen[3]*, Colin Lambert[2]* and Wenjing Hong[1]*

[1]State Key Laboratory of Physical Chemistry of Solid Surfaces, iChEM, College of Chemistry and Chemical Engineering & Pen-Tung Sah Institute of Micro-Nano Science and Technology, Xiamen University, Xiamen, China. [2]Department of Physics, Lancaster University, Lancaster, UK. [3]Shanghai Key Laboratory of Materials Protection and Advanced Materials in Electric Power, Shanghai University of Electric Power, Shanghai, China. [4]Institute of Materials and Environmental Chemistry, Research Centre for Natural Sciences, Hungarian Academy of Sciences, Budapest, Hungary. [5]These authors contributed equally: Jie Bai, Abdalghani Daaoub, Sara Sangtarash, Xiaohui Li. *e-mail: wenbochen@shiep.edu.cn; c.lambert@lancaster.ac.uk; whong@xmu.edu.cn

# Anti-resonance features of destructive quantum interference in single-molecule thiophene junctions achieved by electrochemical gating

**Table of Contents**

# S1. Synthesis

## 1.1 General Information

All commercially available reagents and solvents were obtained from standard chemical suppliers and used without further purification unless otherwise mentioned. Thin-layer chromatography (TLC) analyses were performed on pre-coated 0.25 mm silica plates containing a 254 nm fluorescence indicator. The Flash column chromatograph was carried out using 300-400 mesh silica gel at medium pressure.

NMR spectra were recorded on a Bruker spectrometer and analyzed with the MestReNova Software. ^{1}H NMR spectra were recorded at 400 MHz and chemical shifts are reported in ppm using residual deuterated solvent peak as reference (CDCl$_3$: δ 7.26). Data is reported as follows: chemical shift, multiplicity, coupling constant (*J* in Hz) and integration. The following abbreviations were used to explain the multiplicities: s = singlet, d = doublet, t = triplet, q = quartet, m = multiplet, br = broad. ^{13}C NMR spectra were recorded at 100 MHz using broadband proton decoupling and chemical shifts are reported in ppm relative to residual deuterated solvent peak (CDCl$_3$: δ 77.00). High resolution mass spectra (HRMS) were recorded on a Waters Micromass GCT Premier using EI at 70 eV.

The target molecules were prepared by the Sonogashira coupling[1] of 4-ethynylthioanisole and 1-(thioacetyl)-4-ethynylbenzene with 2,5-dibromothiophene and 2,4-dibromothiophene, respectively. 4-ethynylthioanisole and 1-(thioacetyl)-4-ethynylbenzene were prepared according to published procedures[2, 3].

## 1.2 Synthetic Experimentals
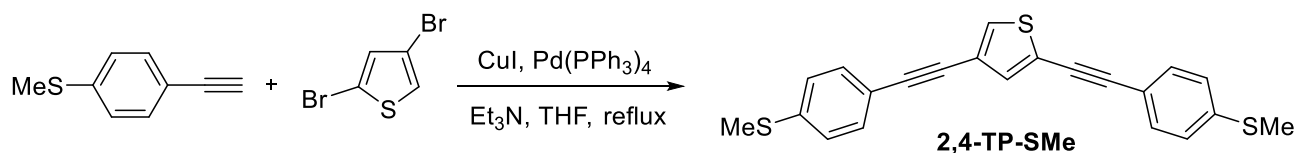


A mixture of compound 2,4-dibromothiophene (223 mg, 0.921 mmol, 1 equiv.), 4-ethynylthioanisole (341 mg, 2.30 mmol, 2.5 equiv.) and degassed Et$_3$N (466 mg, 4.61 mmol, 5 equiv.), Pd(PPh$_3$)$_4$ (106 mg, 0.0917 mmol, 10%), and CuI (17.5 mg, 0.0918 mmol, 10%) in 20.0 mL anhydrous THF was refluxed for 16 h under an argon atmosphere and then cooled to room temperature. The mixture was quenched by water and then extracted with ethyl acetate. The combined organic extract was dried over

anhydrous Na$_2$SO$_4$, filtered and concentrated under reduced pressure. The residue was purified through flash column chromatography by hexane/dichloromethane (10/1) over silica gel to afford **2,4-TP-SMe**. Yield: 202 mg, 58%.

**2,4-bis[4-(thiomethyl)phenylethynyl]thiophene (2,4-TP-SMe)**. White solid. ^{1}H NMR (400 MHz, CDCl$_3$) δ 7.43-7.40 (m, 5H), 7.30 (d, *J* = 1.2 Hz, 1H), 7.22-7.20 (m, 4H), 2.50 (s, 6H); ^{13}C NMR (100 MHz, CDCl$_3$) δ 140.0, 139.5, 133.8, 131.8, 131.7, 129.7, 125.9, 125.8, 123.5, 122.4, 119.1, 118.7, 93.4, 88.8, 83.9, 81.9, 15.4, 15.3; HRMS (EI+) calcd for C$_{22}$H$_{16}$S$_3$: 376.0414; found 376.0415.
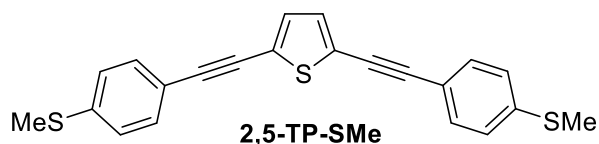


**2,5-TP-SMe**

**2,5-bis[4-(thiomethyl)phenylethynyl]thiophene (2,5-TP-SMe)**. Yellow solid. ^{1}H NMR (400 MHz, CDCl$_3$) δ 7.42 (d, *J* = 8.4 Hz, 4H), 7.20 (d, *J* = 8.4 Hz, 4H), 7.13 (s, 2H), 2.50 (s, 6H); ^{13}C NMR (100 MHz, CDCl$_3$) δ 140.0, 131.7, 125.8, 124.6, 118.7, 94.0, 82.4, 15.3; HRMS (EI+) calcd for C$_{22}$H$_{16}$S$_3$: 376.0414; found 376.0410. The data are consistent with previous report[2].



**2,5-TP-SAc**
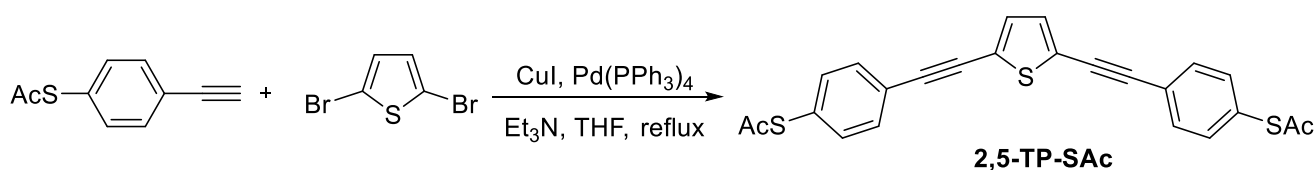
A mixture of compound 1-(thioacetyl)-4-ethynylbenzene (377 mg, 2.14 mmol, 2.12 equiv.), 2,5-dibromothiophene (243 mg, 1.01 mmol, 1 equiv.), Pd(PPh$_3$)$_4$ (115.5 mg, 0.1 mmol, 0.1 equiv.), CuI (19.5 mg, 0.1 mmol, 0.1 equiv.), and degassed Et$_3$N (1 mL) in 20.0 mL of anhydrous THF was refluxed overnight under an argon atmosphere and then cooled to room temperature. The mixture was quenched by water and then extracted with ethyl acetate. The combined organic extract was dried over anhydrous Na$_2$SO$_4$, filtered and concentrated under reduced pressure. The crude product was purified with flash column chromatography by hexane/ethylacetae (15/1) over silica gel to afford **2,5-TP-SAc**. Yield: 120 mg, 28%. The sample was further purified by crystallization for characterization.
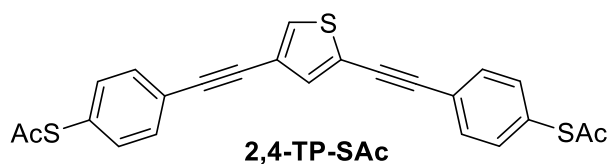
**2,5-bis[4-(acetylthio)phenylethynyl]thiophene (2,5-TP-SAc)**. Pale yellow solid. ^{1}H NMR (400 MHz, CDCl$_3$) δ 7.54 (d, *J* = 8.4 Hz, 4H), 7.40 (d, *J* = 8.8 Hz, 4H), 7.18 (s, 2H), 2.44 (s, 6H); ^{13}C NMR

(100 MHz, CDCl$_3$) δ 193.3, 134.2, 132.2, 132.0, 128.6, 124.6, 123.7, 93.5, 83.8, 30.3; HRMS [M+H]$^+$ calcd for C$_{24}$H$_{17}$O$_2$S$_3$: 433.0385; found 433.0385. The data are consistent with previous report[4].



**2,4-bis[4-(thioacetyl)phenylethynyl]thiophene (2,4-TP-SAc)**. Pale yellow solid. ^{1}H NMR (400 MHz, CDCl$_3$) δ 7.55-7.52 (m, 4H), 7.47 (d, $J$ = 1.6 Hz, 1H), 7.42-7.39 (m, 4H),7.35 (d, $J$ = 1.2 Hz, 1H), 2.44 (s, 6H); ^{13}C NMR (100 MHz, CDCl$_3$) δ 193.4, 193.3, 134.3, 134.2, 132.1, 132.0, 130.6, 128.6, 128.2, 124.1, 123.7, 123.2, 122.1, 92.9, 88.4, 85.3, 83.3, 30.3, 30.2; HRMS [M+H]$^+$ calcd for C$_{24}$H$_{17}$O$_2$S$_3$: 433.0385; found 433.0384. The data are consistent with previous report[4].

# S2. The electrochemically-gated, mechanically controllable break junction technique
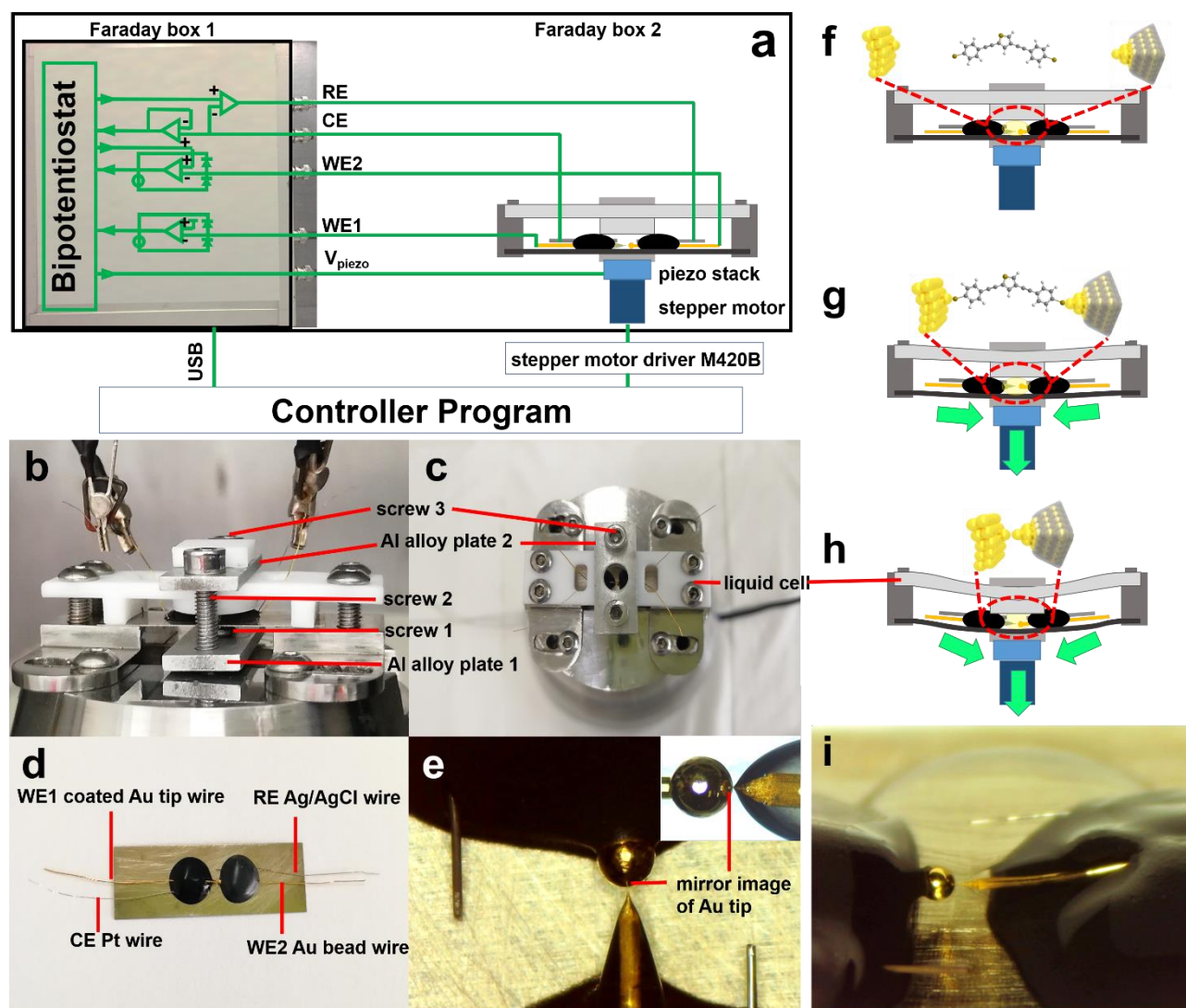


**Supplementary Fig. 1 | Electrochemically-gated, mechanically controllable break junction technique. a**, Schematics of the electrochemically-gated, mechanically controllable break junction technique. **b**, Side-view of the setup. **c**, Top-view of the setup. **d**, Photo of electrochemical tip-bead (ECTB) chip. **e**, Photo of ECTB chip under microscope. Inset: magnified photo of the Au bead and coated Au tip before fixing with epoxy. **f**, "Break" state: Au bead and coated Au tip separated by a submillimetre gap and the liquid cell is flat (on the ECTB chip). **g**, "Junction" state: formation of single-molecule junction in a nanogap and the liquid cell is bent downward slightly. **h**, "Connection" state: Au bead and coated Au tip connected each other and the liquid cell is bent downward further. **i**, Photo of ECTP chip under microscope with electrodes immersed in $HMIPF_6$ ionic liquid.

Supplementary Fig. 1a shows the schematics of the electrochemically-gated, mechanically controllable break junction technique. Electrochemical gating is performed by a four-electrode

bipotentiostat setup, where both the coated Au tip and Au bead serve as the working electrodes. The potential of the working electrodes can be controlled separately with respect to the reference electrode upon the bipotentiostat setup, and the potential difference between the two working electrodes is the bias voltage applied to the molecular junctions. In electrochemical gating measurements, the electrode potentials of coated Au tip and Au bead were tuned simultaneously relative to the Ag/AgCl quasi-reference electrode, and the potential of coated Au tip is 0.1 V higher than that of Au bead all along. In all the experiments, we adopted the potentials of coated Au tip relative to the Ag/AgCl as the applied potentials.

In order to realize the break-junction measurement of ECTB chips, we made significant modifications to the mechanically controllable break junction (MCBJ) setup. Supplementary Fig. 1b and 1c illustrate the profile of the improved setup. A polytetrafluoroethylene (PTFE) liquid cell was placed onto the surface of the ECTB chip and fixed on the cone substrate. Meanwhile, the liquid cell and the ECTB chip were immobilized additionally by two Al alloy plates, the bottom of which was attached to the actuator below. The two Al alloy plates were connected together with two screws.

Supplementary Fig. 1d and 1e display the photos of the ECTB chip. Pt wire (0.1 mm diameter, 99.95%, Jiaming, Beijing) and Ag/AgCl wire were used as the counter and reference electrodes, respectively. Briefly, Ag/AgCl wire was fabricated by electrochemically oxidizing Ag wire (0.1 mm diameter, 99.99%, Jiaming, Beijing) at a constant potential of 1.5 V in the electrolyte of (37% HCl : $H_2O$ = 1:1, v/v). The coated Au tip was prepared by etching a Au wire (0.15 mm diameter, 99.99%, Jiaming, Beijing) in a solution of (37% HCl : ethanol = 1:1, v/v) at a constant potential of 1.2 V and then coated with hot melt adhesive (Ace Hardware Corp., USA). In our study, the Au beads about 0.35-0.50 mm in diameter are prepared by butane flame. The electrodes were fixed to a spring steel sheet (30 mm × 10 mm with 0.15 mm thickness) using two drops of epoxy (Stycast 2850 FT with catalyst 9) as shown in Supplementary Fig. 1d.

Before each experiment, the as-prepared chip was rinsed by isopropanol and dried by natural volatilization. The chip was then placed on the Al alloy plate 1 (which is fixed to the underneath actuator through screw 1) of the MCBJ setup and the PTFE liquid cell was fixed on the top of the chip by screws (Supplementary Fig. 1). Subsequently, the Al alloy plate 2 was mounted on the top of PTFE liquid cell and fixed with Al alloy plate 1 together by screw 2 and screw 3. After that, the thiophene derivatives were prepared to be 0.5 mM in a solvent of $HMIPF_6$ (purchased from lolitec ionic Liquids

Technologies, Germany) and then added 10-15 μL molecular solution to the PTFE liquid cell. The viscous ionic liquid with poor mobility will be stabilized between two epoxy resins, and meanwhile the Au bead and coated Au tip are both immersed entirely in ionic liquid (Supplementary Fig. 1i). Owing to the small distance between coated Au tip and Au bead (submillimetre gap), they will connect when the chip bents down slightly. In such case, the ionic liquid will not leak during the experiments. During the measurements, the ECTB chip was bent with the Al alloy plates, which were driven by a combination of a stepper motor (Zaber NA14B16) and a piezo stack (Thorlab AE0505D18F). Different with the typical notched Au wire chips used in MCBJ technique, the initial distance between coated Au tip and Au bead was adjusted to be less than 50 μm (Supplementary Fig. 1e). Therefore, the actuator below moved down firstly and both the liquid cell and the ECTB chip were thus pulled down by the two Al alloy plates and the micro-scale gap reduced to nanogap that comparable to the target molecular length (Supplementary Fig. 1g). Then the actuator moves further down until reaching the upper limit of the current, resulting in the connecting of the coated Au tip and Au bead electrodes (Supplementary Fig. 1h). Subsequently, the actuator moves up and the connection is broken. The working principle of the ECTB setup is also based on a three–point bending mechanism with horizontal structure like the normal MCBJ technique, and the breaking and connecting process is performed by the controllable bending of ECTB chip like the notched wire chip in normal MCBJ technique[5-7]. During the repeated connecting/breaking process, the evolution of conductance characteristics was recorded for further analysis.

## S3. Cyclic voltammetry measurements
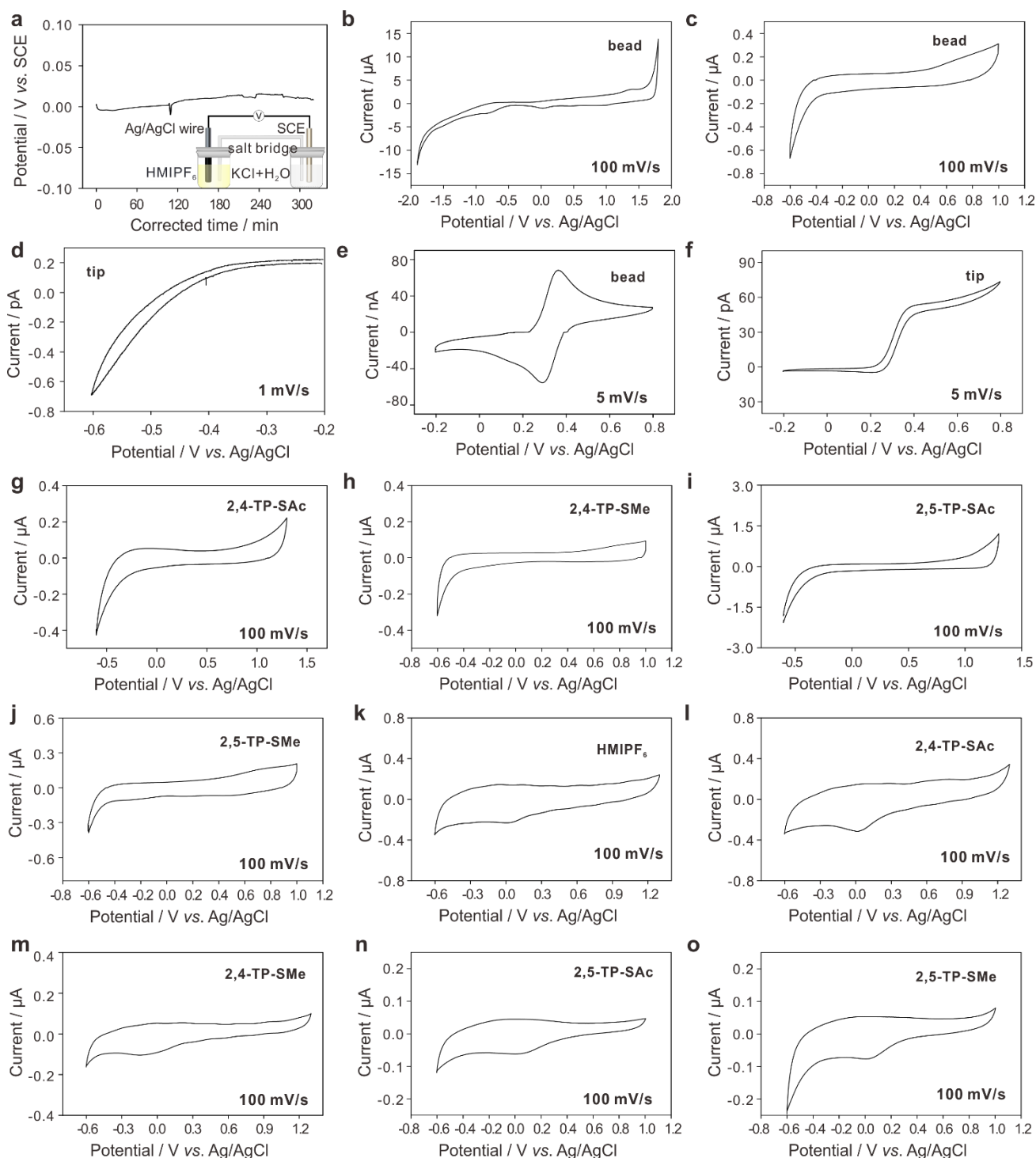


**Supplementary Fig. 2 | Electrochemical measurements. a**, Time-dependence of Ag/AgCl quasi-reference electrode *vs.* SCE with controlled current at 2.98 ± 4.26 pA (inset: schematic of the setup). The oscillation of open-circuit potential was as lower than 15 mV more than 5 hours. **b-j**, Cyclic voltammetry measurements through ECTB chip at ambient conditions. **b**, Whole potential window of HMIPF$_6$ at Au bead. **c**, HMIPF$_6$ in the potential range from −0.6 V to 1.0 V at Au bead. **d**, HMIPF$_6$ in the potential range from −0.6 V to −0.2 V at coated Au tip. **e**, Ferrocene at Au bead. **f**, Ferrocene at

8

coated Au tip. **g**, **2,4-TP-SAc**. **h**, **2,4-TP-SMe**. **i**, **2,5-TP-SAc**. **j**, **2,5-TP-SMe**. Working electrode: Au bead, reference electrode: Ag/AgCl wire, counter electrode: Pt wire. **k-o**, Cyclic voltammetry measurements of $HMIPF_6$ and 0.5 mM thiophene derivatives in $HMIPF_6$ in glovebox saturated with argon. **k**, Pure $HMIPF_6$. **l**, **2,4-TP-SAc**. **m**, **2,4-TP-SMe**. **n**, **2,5-TP-SAc**. **o**, **2,5-TP-SMe**. Working electrode: Au bead, reference electrode: Ag/AgCl wire, counter electrode: Pt wire.

Before the electrochemical experiments, the stability of the Ag/AgCl quasi-reference electrode was tested by open-circuit potential measurements using two-electrode system[8] (Supplementary Fig. 2a inset). The working electrode and the reference electrode were the Ag/AgCl quasi-reference electrode and a commercial saturated calomel electrode (SCE, CH Instruments Inc.), respectively. The two electrodes were placed separately (Ag/AgCl quasi-reference electrode was placed in the $HMIPF_6$ ionic liquid, and SCE was placed in a saturated KCl aqueous solution) and connected through an agar-$KNO_3$-$HMIPF_6$ filled salt bridge. The potential signal outputs of the two electrodes were recorded through an Autolab electrochemical workstation (Eco Chemie, Netherlands). Supplementary Fig. 2a shows the time-dependence of Ag/AgCl quasi-reference electrode *vs.* SCE with controlled current at $2.98 \pm 4.26$ pA. The oscillation of open-circuit potential is as low as 10 mV in the first 2 hours, and less than 15 mV for more than 5 hours. For our experiments, all the conductance measurements were performed within 5 hours. Since the potential difference within 5 hours (maximum 15 mV) is significantly lower than the potential difference that we applied between each data points (200 mV), we can conclude that the Ag/AgCl quasi-reference electrode is sufficiently stable for the electrochemical gating experiments.

Supplementary Fig. 2b shows the potential window of the $HMIPF_6$ at the Au bead working electrode. The $HMIPF_6$ will decompose at the potential higher than 1.8 V and lower than $-1.9$ V vs. Ag/AgCl, indicating the potential window of $HMIPF_6$ was 3.7 V at ambient conditions. However, two additional peaks (at 0 V and $-0.6$ V) can be found using a sensitive scale in the potential window. Actually, the CVs of ionic liquids were not flat on a sensitive current scale, and the peaks mainly corresponded to the interfacial behaviour of ions during the charging and adsorption processes[9-11]. Considering the polycrystal of the Au bead, the charging and adsorption process of ions are different at different crystal faces of the Au. The peak around 0 V, was also found in a previous report of 1-butyl-3-methyl-imidazolium hexafluorophosphate ($BMIPF_6$) ionic liquid[9], which they ascribed to the complete re-orientation of the double layer. It should be noticed that the peak at 0 V did not appear when scanning

in a narrow potential window from −0.6 V to 1.0 V. As to the peak around −0.6 V, it is mostly attributed to the decomposition of the trace water, which is inevitable at ambient conditions. To examine the influence of Faraday current on the increasing conductance at −0.6V, we carried out a cyclic voltammetry measurement at coated Au tip with relative slow scan rate at 1.0 mV/s, as shown in Supplementary Fig. 2d. The cyclic voltammetry demonstrates that the difference of Faraday current at −0.4 V and −0.6 V is lower than 1 pA. In the gating experiments, we have measured the conductance at each potential for more than 20 minutes (< 0.1 mV/s) that we would expect the faraday current was even lower.

To test the feasibility of the chip for electrochemical measurements, we measured the cyclic voltammogram (CV) in HMIPF$_6$ containing 1.0 mM ferrocene probe through MCBJ bipotentiostat at ambient conditions (Supplementary Fig. 2e and 2f). A couple of well-defined redox peaks of ferrocene with the formal potential of 0.33 V was observed when the Au bead acted as the working electrode, while a sigmoid-shaped CV curve corresponding to semi-infinite spherical diffusion processes with the charging current of about 3.0 pA was obtained at the coated Au tip, indicating that the exposed area of the Au tip was decreased dramatically after coating.

CV measurements of **2,4-TP-SAc** and **2,5-TP-SAc** were carried out on ECTB chips in the electrolyte of HMIPF$_6$ containing 0.5 mM target molecule through MCBJ bipotentiostat at ambient conditions. The Au bead was used as the working electrode, and the Ag/AgCl wire and Pt wire were used as the reference and counter electrodes, respectively. As shown in supplementary Fig. 2g and 2i, no redox peaks were found from −0.6 to 1.3 V for both **2,4-TP-SAc** and **2,5-TP-SAc**, indicating the potential range from −0.6 to 1.3 V is a non-faradaic region. The different values of charging currents were mainly caused by the different electrode surface areas. Actually, the surface areas of the Au bead electrodes are different from each other. On the one hand, the size of the Au beads is influenced significantly by the annealing process of the Au wires, which is difficult to control precisely. On the other hand, the epoxy resin before solidification would float and cover the Au bead partly during the fabrication of ECTB chips, thus decreasing the electrode area.

Supplementary Fig. 2k shows the CV curves of pure HMIPF$_6$ measured in glovebox filled with ultra-pure argon through an Autolab electrochemical workstation (Eco Chemie, Netherlands). A peak was found at around 0 V at a sensitive current scale. Considering such low current density (about $10^{-3}$ mA cm$^{-2}$), it is most likely the characteristic of the ionic liquid molecules on the charged Au surface, which

has been also reported in previous papers[9,10]. This peak can be found in all CV curves of the thiophene derivative molecular solutions under argon atmosphere, however, they disappeared under ambient conditions. Apart from this peak, no redox peaks corresponding to the thiophene core were obtained between −0.6 V to 1.3 V for both **2,4-TP-SAc** and **2,5-TP-SAc**, which was in accordance with those at ambient conditions.

## S4. Single-molecule conductance characterization

### 4.1 Construction of the conductance histograms

During the repeated connecting/breaking process, the evolution of conductance characteristics was recorded by a logarithmic $I$-$V$ converter with a sampling rate of 10 $k$Hz using microcontroller for data acquisition. Details about the construction of the histograms are described as follows: 1D histograms are plotted on a logarithmic conductance scale without background subtraction and the conductance bin size is 0.01 log $(G/G_0)$. The feature around $-7$ log $(G/G_0)$ represents the noise level (Supplementary Fig. 3b). The most probable conductance value is determined by a Gaussian fit. In the 2D conductance–displacement histograms, the Y-axis is constructed by taking the logarithm of the conductance value and the bin size is 0.01 log $(G/G_0)$. The determination of the X-axis is based on the linear relationship between the logarithmic conductance and distance of working electrodes[12,13]. By setting a relative zero position at $-0.3$ log $(G/G_0)$[14]. The displacement is obtained from the formula $\Delta z = \text{piezo rate} \times \text{sampling rate} \times N_{data}$, where the piezo rate is the stretching rate calibrated from a pure solvent experiment, with a sampling rate is 10 $k$Hz, and $N_{data}$ is the number of data points. The bin size for the X-axis is 0.007 nm. The resulting 2D conductance–displacement histograms are plotted as intensity graphs based on the data number density in the bins. We constructed the relative displacement distributions by calculating the relative displacement from the relative zero position at $-0.3$ log $(G/G_0)$ to the lower limit conductance of molecular junctions, which is defined as one order of magnitude lower than the most probable conductance. The bin size for the relative displacement distributions is 0.007 nm, and 1100 bins are used for the whole conductance range from $10^1$ $G_0$ to $10^{-10}$ $G_0$. The data analysis is based on a lab-made program implemented in LabVIEW 2016 and all the data recorded in the breaking process are used.
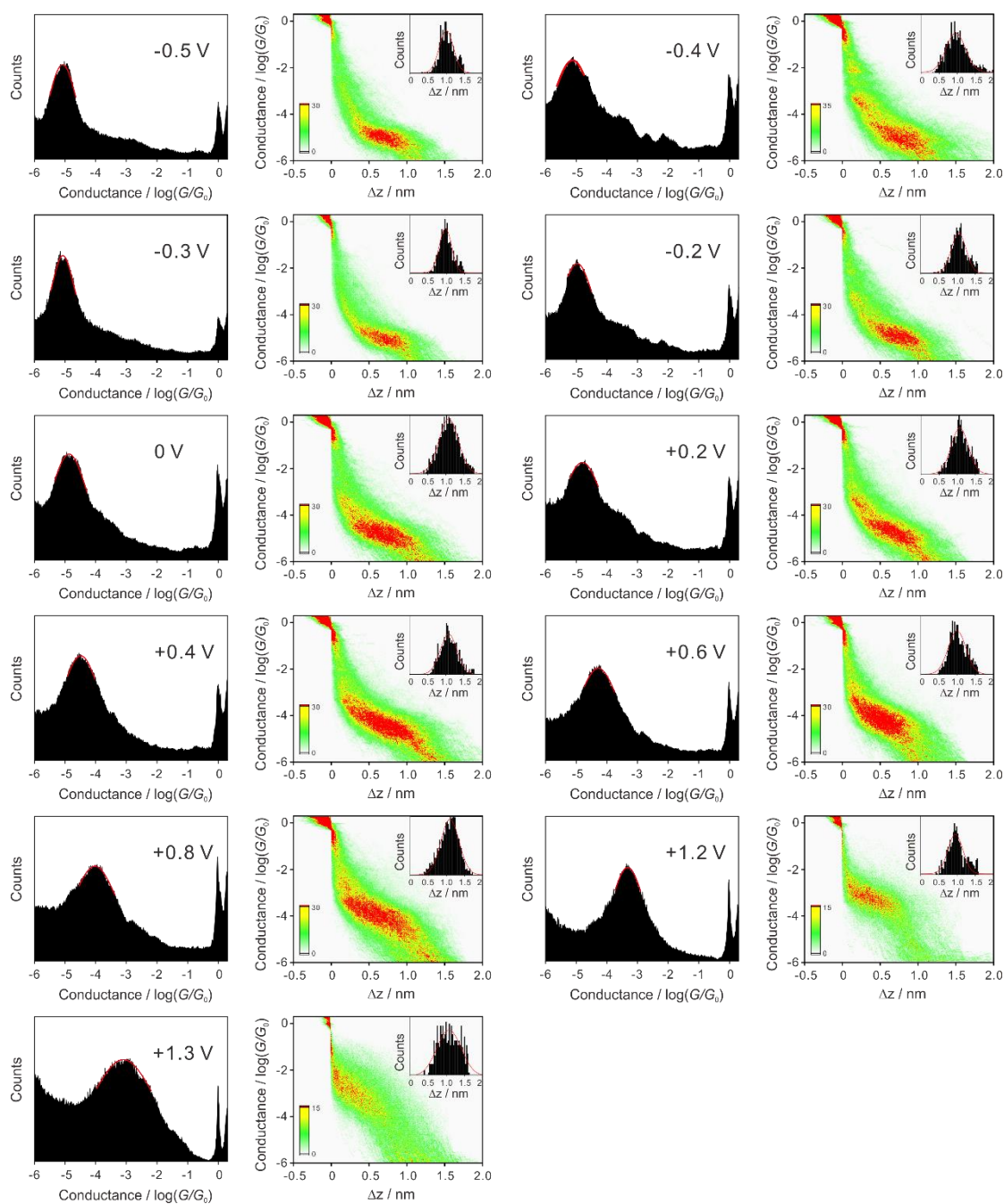
## 4.2 Calibration of the distance measurements
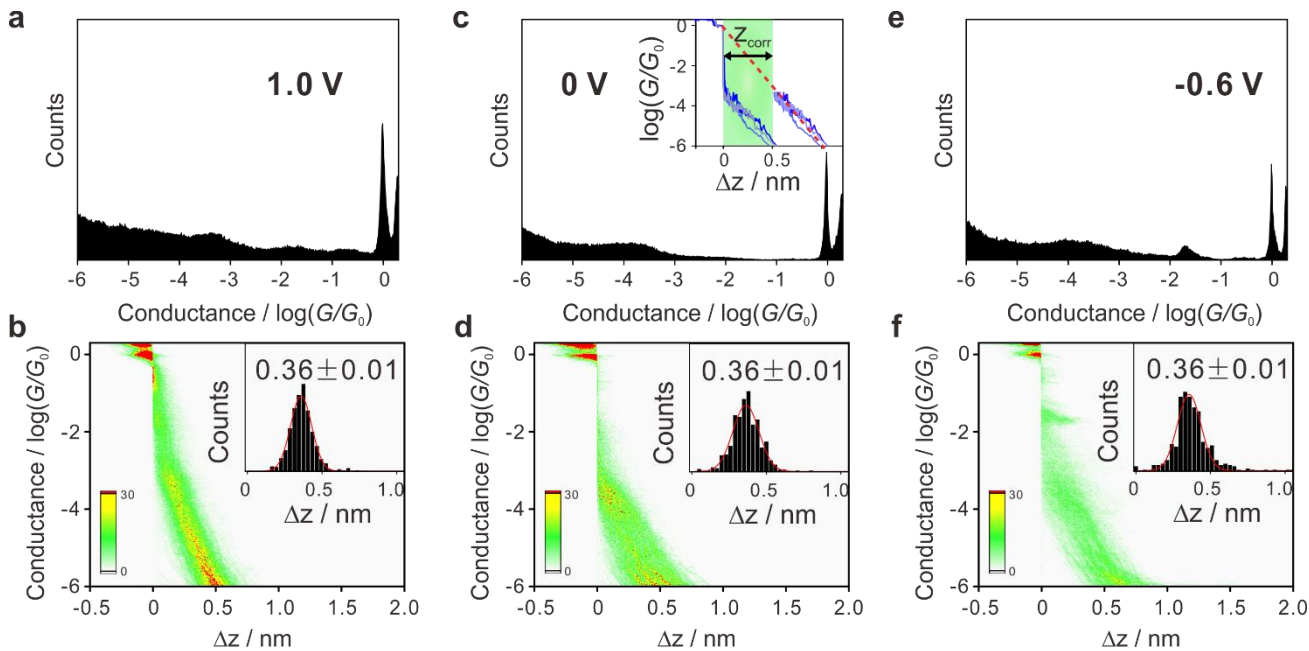


**Supplementary Fig. 3 | 1D and 2D conductance histograms (inset: the relative displacement distributions ranging from $10^{-4}$ to $10^{-6}$ $G_0$) of HMIPF$_6$ measured in the selected potentials.** Inset of Fig. 3b illustrates the estimation of the snap-back distance. Clean background in 1D conductance histograms (**a-c**) and the direct tunnelling characteristic in 2D conductance histograms (**d-f**) suggested that no single-molecule junction was formed during the experiment measurements in pure solvent of HMIPF$_6$.

To determine the calibration of the distance measurements, we calculate the stretching rate and snap-back distance of the ECTB chip, as we reported previously[15-17]. As shown in Supplementary Fig. 3, after the rupture of Au-Au contact, the conductance decreases sharply from 1 $G_0$ to approximately $10^{-3}$ $G_0$, and the distance between the tip-bead electrodes $z$ increases instantaneously to the snap-back distance $z_{corr}$, because of the snap-back effect. In blank experiment of pure solvent, the tunnelling equation is given as $G = G_0 e^{-\beta_T z}$, where $\beta_T$ is the tunneling decay constant in units of length$^{-1}$. The above tunnelling equation can be transferred to $\log(G/G_0) = -0.434\beta_T z$. Since we measured distance in experiment directly is the relative distance $\Delta z = z - z_{corr}$. Then a plot of $\log(G/G_0)$ versus $\Delta z$ has a slope of $-0.434\beta_T$ and an intercept of $0.434\beta_T z_{corr}$. Subsequently the decay constant $\log(\Delta G/G_0)/\Delta z = -5.5$ nm$^{-1}$ [7,17] was used to scale the linear distance distribution from $10^{-4}$ $G_0$ to $10^{-6}$ $G_0$ which should be 0.36 nm (2/5.5 nm$^{-1}$). By calibrating the relative distance distribution from $10^{-4}$ $G_0$ to $10^{-6}$ $G_0$ to 0.36 nm, the stretching rate (also known as piezo rate in units of nm/data) was

determined and used for further analysis of the 2D conductance histograms and the relative displacement distributions of the molecular junctions. The snap-back distance was estimated from the breaking point to the full relaxation of the process and was determined to be 0.50 nm as shown in the inset of Supplementary Fig. 4b. The value of the snap-back distance is in good agreement with a previous report[18]. The most probable absolute stretching distance $z = \Delta z + z_{corr}$ was determined by the correction with the snap-back distance $z_{corr} = 0.5$ nm. In our measurement, the distance is determined directly from the tunnelling current other than the piezo traveling distance or the reduction ratio from sample to sample. Thus the variation in the mechanical reduction ratio will not influence the calibration of the distance measurements as we have discussed.

## 4.3 Conductance histograms and relative displacement distributions of thiophene derivatives



**Supplementary Fig. 4 | 1D and 2D conductance histograms (inset: the relative displacement distributions) of 2,4-TP-SAc measured in the potential range of −0.5 V to 1.3 V.**
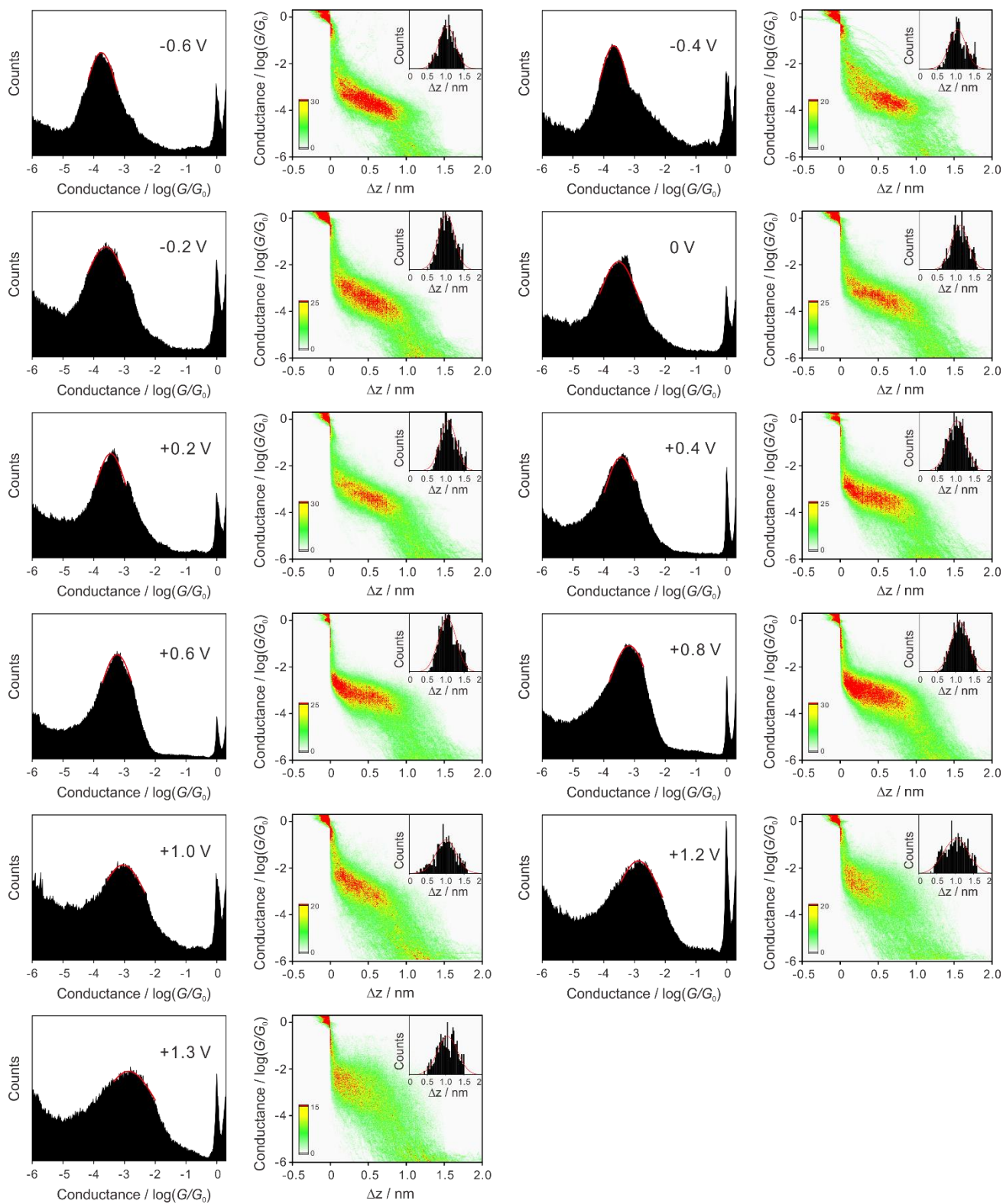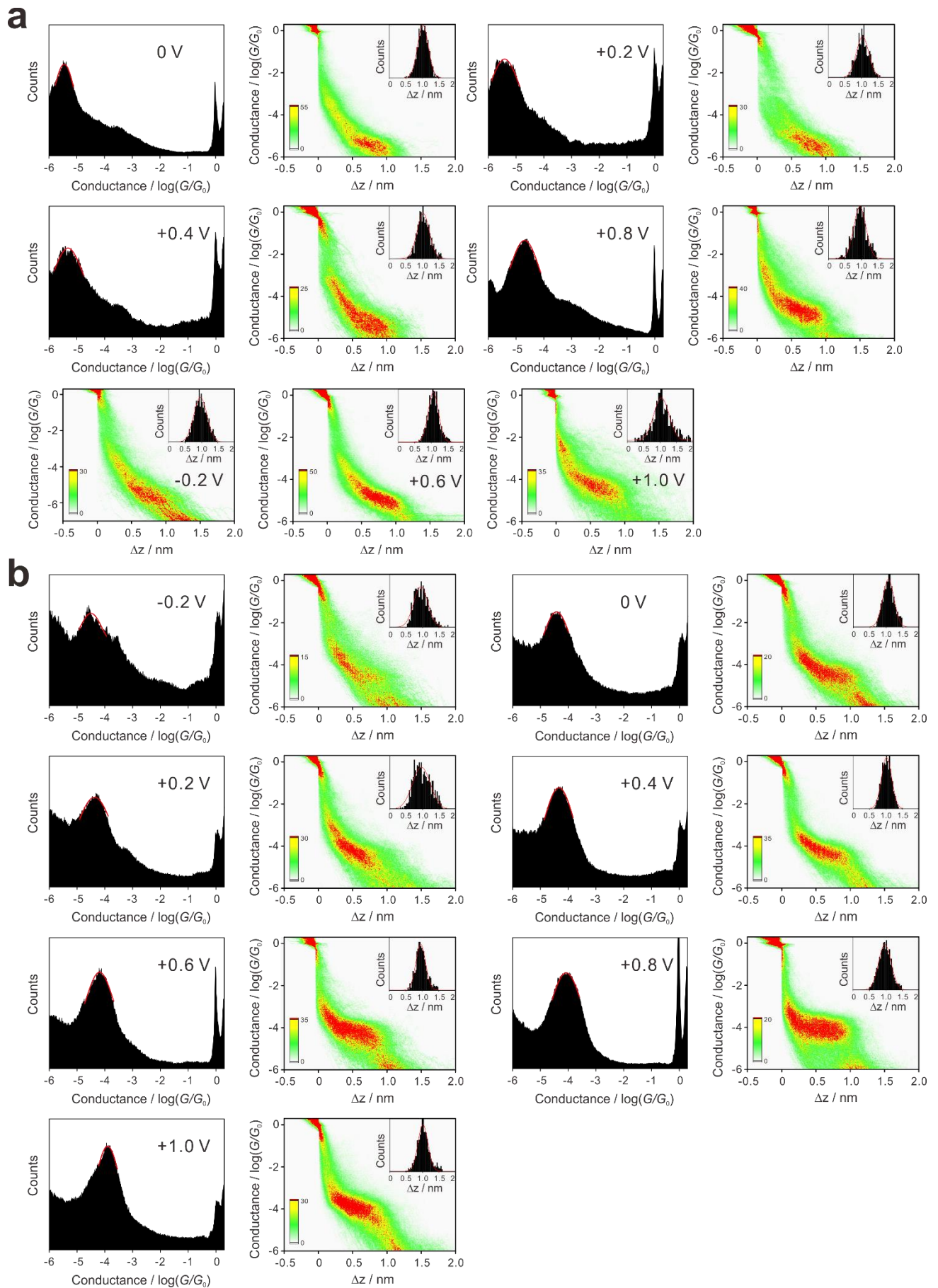
**Supplementary Fig. 5 | 1D and 2D conductance histograms (inset: the relative displacement distributions) of 2,5-TP-SAc measured in the potential range of −0.6 V to 1.3 V.**

**Supplementary Fig. 6 | 1D and 2D conductance histograms (inset: the relative displacement**

**distributions) of 2,4-TP-SMe and 2,5-TP-SMe. a**, 1D and 2D conductance histograms (inset: the relative displacement distributions) of **2,4-TP-SMe** measured in the potential range of 0 V to 0.8 V, and 2D conductance histograms (inset: the relative displacement distributions) of **2,4-TP-SMe** measured at −0.2 V, 0.6 V and 1.0 V. **b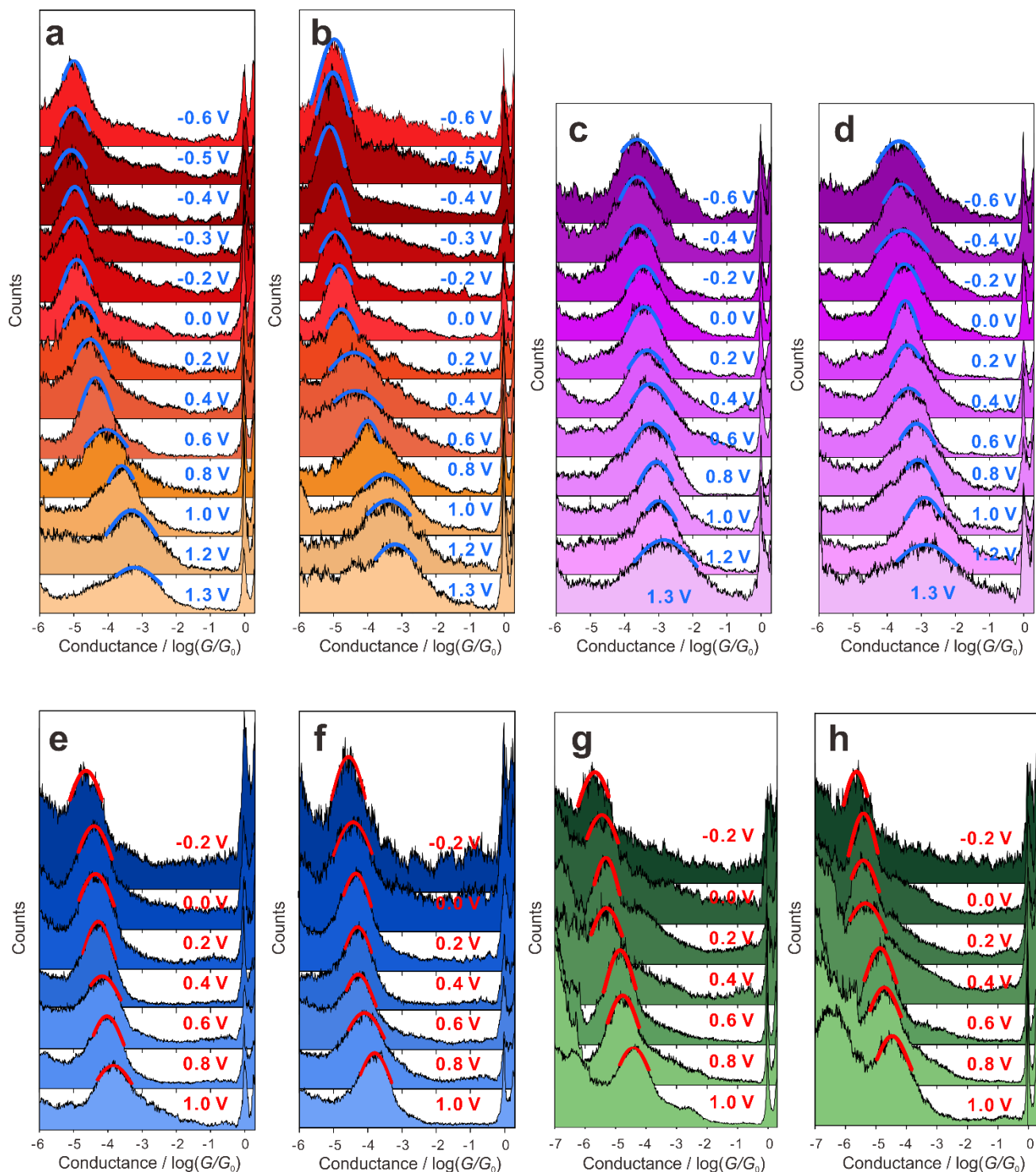**, 1D and 2D conductance histograms (inset: the relative displacement distributions) of **2,5-TP-SMe** measured in the potential range of −0.2 V to 1.0 V.
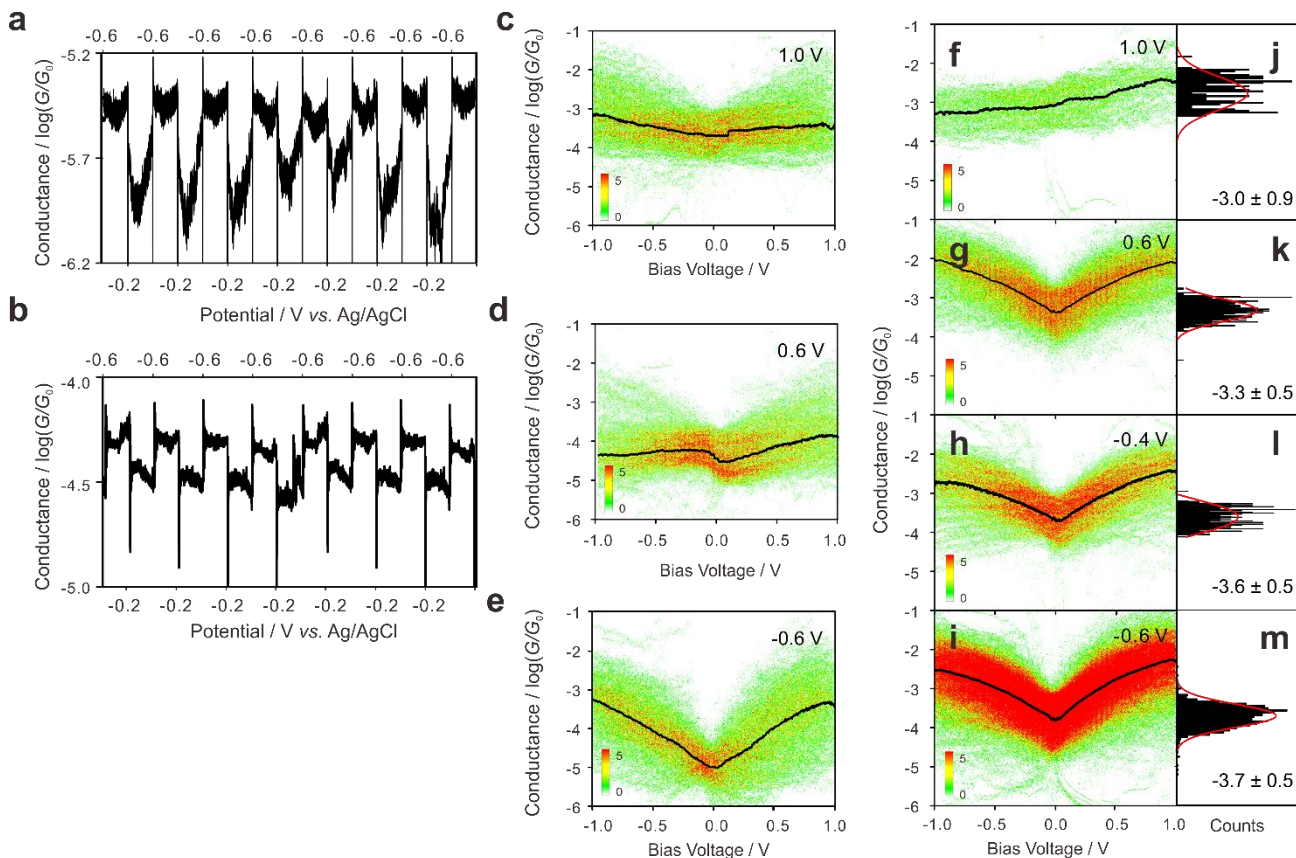


**Supplementary Fig. 7 | 1D conductance histograms of the other two independent conductance**

measurements besides the experiments presented in Supplementary Fig. 4-6. **a**, **b**, **2,4-TP-SAc** from the −0.6 V to 1.3 V. **c**, **d**, **2,5-TP-SAc** from the −0.6 V to 1.3 V. **e**, **f**, **2,5-TP-SMe** from the −0.2 V to 1.0 V. **g**, **h**, **2,4-TP-SMe** from the −0.2 V to 1.0 V.



**Supplementary Fig. 8 | Conductance-electrode potential measurements and current/ conductance-voltage measurements. a**, Typical individual conductance-electrode potential traces of **2,4-TP-SAc** when the gate voltage sweeps between −0.2 and −0.6 V at 1 V/s with fixed bias voltage 100 mV between the two electrodes. **b**, Typical individual conductance-electrode potential traces of **2,5-TP-SAc** when the gate voltage sweeps between −0.2 and −0.6 V at 1 V/s with fixed bias voltage 100 mV between the two electrodes. **c-e**, 2D current/conductance-voltage histogram of **2,4-TP-SAc** at 1.0 V with 335 curves, 0.6 V with 406 curves and −0.6 V with 359 curves. **f-g**, 2D current/conductance-voltage histogram of **2,5-TP-SAc** at 1.0 V with 135 curves, 0.6 V with 615 curves, −0.4 V with 474 curves and −0.6 V with 1649 curves. **j-m**, Conductance distributions of **2,5-TP-SAc** at 1.0 V, 0.6 V, −0.4 V and −0.6 V determined from the slopes from −100 mV to 100 mV. The error bars of the conductance value were determined from the peak width at half maximum from Gauss fitting. The 2D histograms of current/conductance-voltage were constructed with a bin size of 1000 × 1000 in 2D space and the bin size of conductance distributions of low-bias conductance is 0.03 log
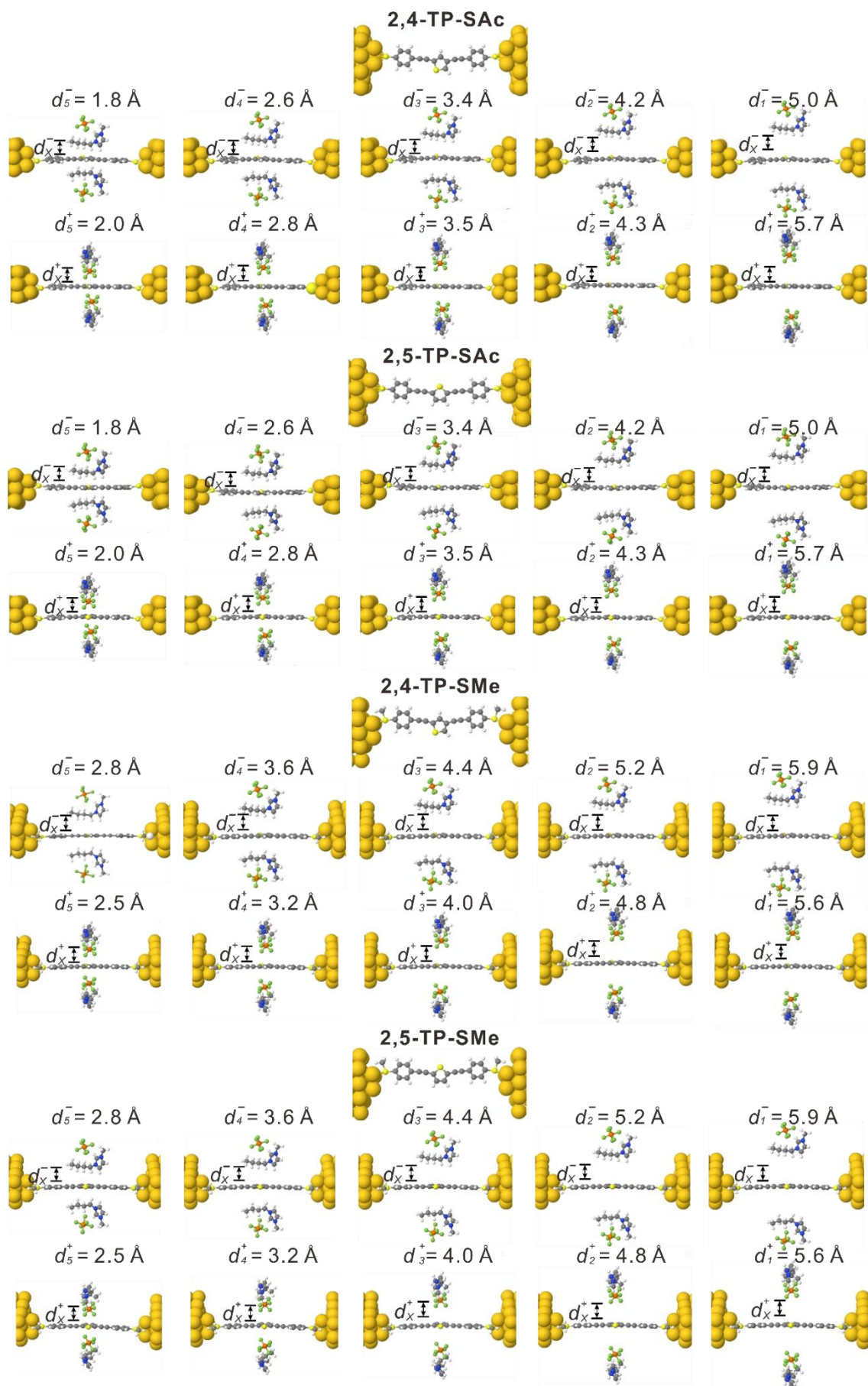
$(G/G_0)$.

## S5. Theoretical modelling

**DFT calculations:** The optimized geometry, ground state Hamiltonian and overlap matrix elements of each structure were self-consistently obtained using the SIESTA[19] implementation of density functional theory (DFT). SIESTA employs norm-conserving pseudo-potentials to account for the core electrons and linear combinations of atomic orbitals to construct the valence states. The generalized gradient approximation (GGA) of the exchange and correlation functional is used with the Perdew-Burke-Ernzerhof parameterization (PBE) a double-$\zeta$ polarized (DZP) basis set, a real-space grid defined with an equivalent energy cut-off of 250 Ry. The geometry optimization for each structure is performed to the forces smaller than 10 meV/Å.

**Transport calculations:** The mean-field Hamiltonian obtained from the converged DFT calculation was combined with Gollum quantum transport code[20,21] to calculate the phase-coherent, elastic scattering properties of the each system consist of left Au (source) and right Au (drain) leads and the scattering region. The transmission coefficient $T(E)$ for electrons of energy $E$ (passing from the source to the drain) is calculated via the relation: $T(E) = Trace(\Gamma_R(E)G^R(E)\Gamma_L(E)G^{R\dagger}(E))$. In this expression, $\Gamma_{L,R}(E) = i\left(\sum_{L,R}(E) - \sum_{L,R}{}^{\dagger}(E)\right)$ describe the level broadening due to the coupling between left (L) and right (R) electrodes and the central scattering region, $\sum_{L,R}(E)$ are the retarded self-energies associated with this coupling and $G^R = (ES - H - \sum_L - \sum_R)^{-1}$ is the retarded Green's function, where $H$ is the Hamiltonian and $S$ is overlap matrix. Using obtained transmission coefficient $T(E)$, the conductance could be calculated by Landauer formula ($G = G_0 \int dE\ T(E)(-\partial f/\partial E)$) where $G_0 = 2e^2/h$ is conductance quantum.

**Calculations of -SMe terminated molecules:** We also carried out the transport calculations for molecules terminated with -SMe (see Supplementary Fig. 10), and found a smaller conductance variation than that of molecules terminated with -SAc, which agrees well with the experiments. The small conductance variation is because both the -SAc and the -SMe-terminated molecules have similar on-resonance transmissions, of order unity, but the off-transmission coefficient of the former is lower than that of the latter, which leads to the stronger gating effect of -SAc compared with the –SMe. This higher off-transmission of -SMe-terminated molecules aries, because although there is perfect destructive interference in the π-channel, there remains a small contribution to the transmission from

the σ-channel, which is larger for -SMe than for –SAc terminated molecules.

**2,4-TP-SAc**



$d_5^- = 1.8$ Å    $d_4^- = 2.6$ Å    $d_3^- = 3.4$ Å    $d_2^- = 4.2$ Å    $d_1^- = 5.0$ Å

$d_5^+ = 2.0$ Å    $d_4^+ = 2.8$ Å    $d_3^+ = 3.5$ Å    $d_2^+ = 4.3$ Å    $d_1^+ = 5.7$ Å

**2,5-TP-SAc**



$d_5^- = 1.8$ Å    $d_4^- = 2.6$ Å    $d_3^- = 3.4$ Å    $d_2^- = 4.2$ Å    $d_1^- = 5.0$ Å

$d_5^+ = 2.0$ Å    $d_4^+ = 2.8$ Å    $d_3^+ = 3.5$ Å    $d_2^+ = 4.3$ Å    $d_1^+ = 5.7$ Å

**2,4-TP-SMe**



$d_5^- = 2.8$ Å    $d_4^- = 3.6$ Å    $d_3^- = 4.4$ Å    $d_2^- = 5.2$ Å    $d_1^- = 5.9$ Å

$d_5^+ = 2.5$ Å    $d_4^+ = 3.2$ Å    $d_3^+ = 4.0$ Å    $d_2^+ = 4.8$ Å    $d_1^+ = 5.6$ Å

**2,5-TP-SMe**



$d_5^- = 2.8$ Å    $d_4^- = 3.6$ Å    $d_3^- = 4.4$ Å    $d_2^- = 5.2$ Å    $d_1^- = 5.9$ Å

$d_5^+ = 2.5$ Å    $d_4^+ = 3.2$ Å    $d_3^+ = 4.0$ Å    $d_2^+ = 4.8$ Å    $d_1^+ = 5.6$ Å

**Supplementary Fig. 9 | Molecular junctions formed by TP connected to the Au electrodes from 2,4 and 2,5 connectivities ended with thiol and –SMe and molecular structures in the presence of HMIFP₆ with different positions.**
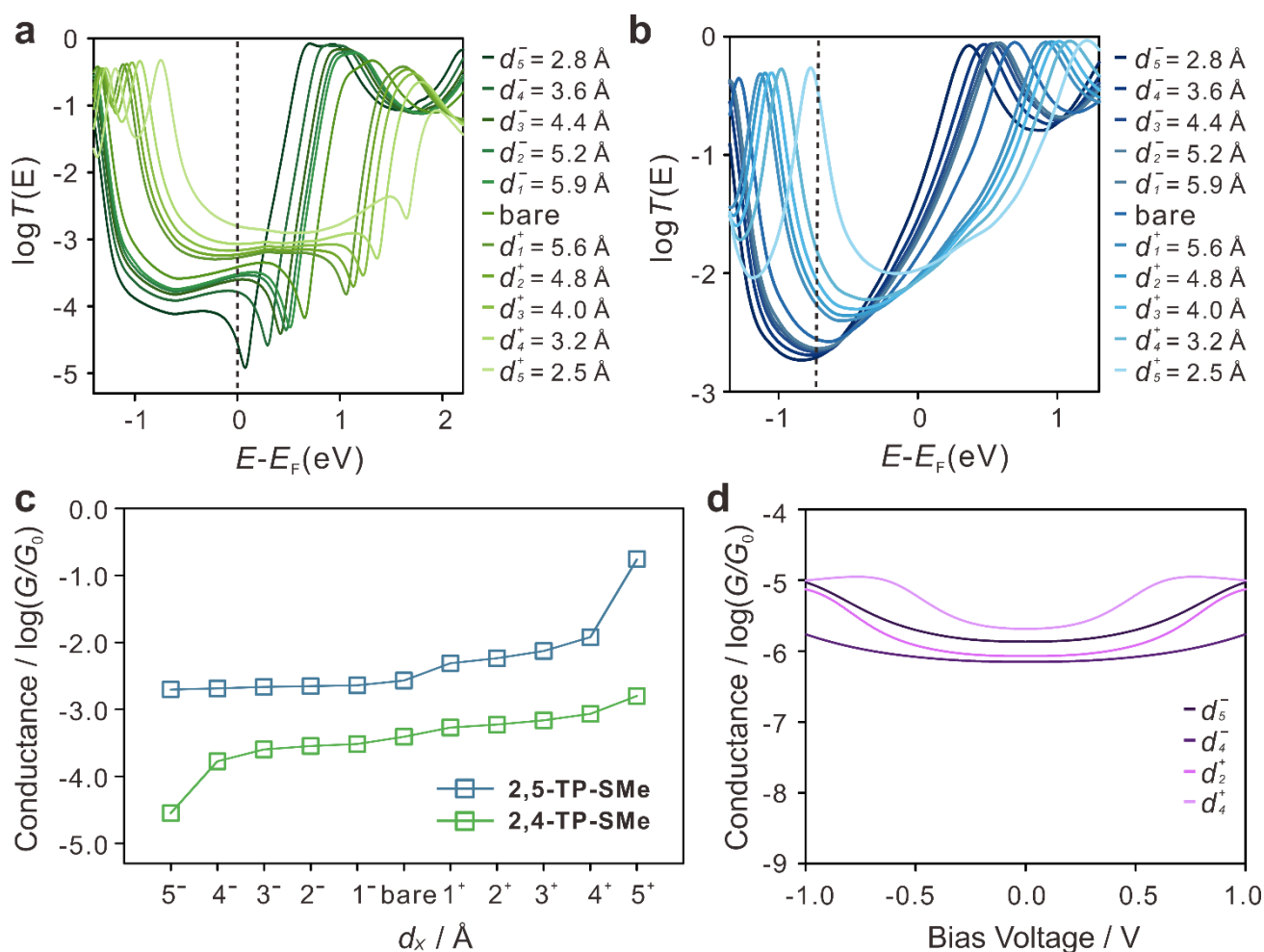


**Supplementary Fig. 10 | a**, Transmission coefficients of **2,4-TP-SMe** in presence of negative and positive charges with different positions. **b**, Transmission coefficients of **2,5-TP-SMe** in presence of negative and positive charges with different positions. **c**, Comparison of **2,4-TP-SMe** and **2,5-TP-SMe** conductance versus the position of HMIPF₆. The Fermi energy (black dashed line) lies at 0 eV for **2,4-TP-SMe** and −0.7 eV for **2,5-TP-SMe**. **d**, Calculated conductance versus bias voltage of **2,5-TP-SAc** for different positions of HMIPF₆.

# References

1. Sonogashira, K., Tohda, Y. & Hagihara, N. A convenient synthesis of acetylenes: Catalytic substitutions of acetylenic hydrogen with bromoalkenes, iodoarenes and bromopyridines. *Tetrahedron Lett.* **16**, 4467-4470 (1975).

2. Miguel, D. *et al.* Toward multiple conductance pathways with heterocycle-based oligo(phenyleneethynylene) derivatives. *J. Am. Chem. Soc.* **137**, 13818-13826 (2015).

3. Liu, K., Wang, X. & Wang, F. Probing charge transport of ruthenium-complex-based molecular wires at the single-molecule level. *ACS Nano* **2**, 2315-2323 (2008).

4. Seidler, A. *et al.* The synthesis of π-electron molecular rods with a thiophene or thieno[3,2-b]thiophene core unit and sulfur alligator clips. *Tetrahedron Lett.* **54**, 2795-2798 (2013).

5. Huang, C. *et al.* Single-molecule detection of dihydroazulene photo-thermal reaction using break junction technique. *Nat. Commun.* **8**, 15436 (2017).

6. Hong, W. *et al.* Trimethylsilyl-terminated oligo(phenylene ethynylene)s: An approach to single-molecule junctions with covalent Au-C sigma-bonds. *J. Am. Chem. Soc.* **134**, 19425-19431 (2012).

7. Hong, W. *et al.* An MCBJ case study: The influence of pi-conjugation on the single-molecule conductance at a solid/liquid interface. *Beilstein J. Nanotechnol.* **2**, 699-713 (2011).

8. Shitanda, I., Kiryu, H. & Itagaki, M. Improvement in the long-term stability of screen-printed planar type solid-state ag/agcl reference electrode by introducing poly(dimethylsiloxane) liquid junction. *Electrochim. Acta* **58**, 528-531 (2011).

9. Gnahm, M., Pajkossy, T. & Kolb, D. M. The interface between Au(111) and an ionic liquid. *Electrochim. Acta* **55**, 6212-6217 (2010).

10. Pajkossy, T. & Kolb, D. M. The interfacial capacitance of Au(100) in an ionic liquid, 1-butyl-3-methyl-imidazolium hexafluorophosphate. *Electrochem. Commun.* **13**, 284-286 (2011).

11. Su, Y., Yan, J., Li, M., Zhang, M. & Mao, B. Electric double layer of Au(100)/imidazolium-based ionic liquids interface: Effect of cation size. *J. Phys. Chem. C* **117**, 205-212 (2013).

12. Huber, R. *et al.* Electrical conductance of conjugated oligomers at the single molecule level. *J. Am. Chem. Soc.* **130**, 1080-1084 (2008).

13. Wu, S. *et al.* Molecular junctions based on aromatic coupling. *Nat. Nanotechnol.* **3**, 569-574 (2008).

14. Liu, J. *et al.* Radical-enhanced charge transport in single-molecule phenothiazine electrical junctions. *Angew. Chem. Int. Ed.* **56**, 13061-13065 (2017).

15. Hong, W. *et al.* Single molecular conductance of tolanes: Experimental and theoretical study on the junction evolution dependent on the anchoring group. *J. Am. Chem. Soc.* **134**, 2292-2304 (2012).

16. O'Driscoll, L. J. *et al.* Electrochemical control of the single molecule conductance of a conjugated bis(pyrrolo)tetrathiafulvalene based molecular switch. *Chem. Sci.* **8**, 6123-6130 (2017).

17. Li, Y. *et al.* Three-state single-molecule naphthalenediimide switch: Integration of a pendant redox unit for conductance tuning. *Angew. Chem. Int. Ed.* **54**, 13586-13589 (2015).

18. Moreno-García, P. *et al.* Single-molecule conductance of functionalized oligoynes: Length dependence and junction evolution. *J. Am. Chem. Soc.* **135**, 12228-12240 (2013).

19. José, M. S. *et al.* The SIESTA method for *ab* initio order-N materials simulation. *J. Phys-Condens. Mat.* **14**, 2745-2779 (2002).

20. Ferrer, J. *et al.* Gollum: A next-generation simulation tool for electron, thermal and spin transport. *New J. Phys.* **16**, 093029 (2014).

21. Hatef, S. Theory of electron, phonon and spin transport in nanoscale quantum devices. *Nanotechnology* **29**, 373001 (2018).